

1 **EDDA 2.0: integrated simulation of debris flow initiation and dynamics,**
2 **considering two initiation mechanisms**

3

4 Ping Shen^a, Limin Zhang^{a *}, Hongxin Chen^b, Ruilin Fan^a

5

6 * Corresponding author.

7 Email address: pshen@connect.ust.hk (P. Shen), cezhangl@ust.hk (L. M. Zhang),

8 chenhongxin@tongji.edu.cn (H. X. Chen), rfanaa@connect.ust.hk (R. L. Fan)

9 ^a Department of Civil and Environmental Engineering, The Hong Kong University of Science
10 and Technology, Clear Water Bay, Hong Kong

11 ^b Key Laboratory of Geotechnical and Underground Engineering of Ministry of Education,
12 Department of Geotechnical Engineering, Tongji University, China.

13 **Abstract:** Climate change results in more frequent rainstorms and more rain-induced debris
14 flows in mountainous areas. The prediction of likely hazard zones is important for debris
15 flow risk assessment and management. Existing numerical methods for debris flow analysis
16 often require the input of hydrographs at prescribed initiation locations, ignoring the initiation
17 process and leading to large uncertainties in debris flow initiation locations, times and
18 volumes when applied to regional debris flow analysis. The evolution of the flowing mixture
19 in time and space is hardly addressed either. This paper presents a new integrated numerical
20 model, EDDA 2.0, to simulate the whole process of debris-flow initiation, motion,
21 entrainment, deposition and property changes. Two physical initiation mechanisms are
22 modeled: transformation from slope failures and surface erosion. Three numerical tests and
23 field application to a catastrophic debris flow event are conducted to verify the model
24 components and evaluate the model performance. The results indicate that the integrated
25 model is capable of simulating the initiation and subsequent flowing process of rain-induced
26 debris flows, as well as the physical evolution of the flowing mixture. The integrated model
27 provides a powerful tool for analyzing multi-hazard processes, hazard interactions and
28 regional debris-flow risk assessment in the future.

29

30 **Keywords:** debris flow; numerical modeling; rainfall infiltration; slope stability; erosion;
31 entrainment.

32 **1 Introduction**

33 Debris flows are one of the most catastrophic hazards in mountainous areas (e.g. Zhang
34 et al., 2013; Raia et al., 2014), and can pose high risks to society (e.g. Tang et al., 2011; Gao
35 et al., 2016). They are often triggered by heavy rainfall and sensitive to climate change (e.g.
36 Wong, 2009; Lee et al., 2010). As extreme rainstorms become more frequent, coping with
37 rain-induced debris flows thus becomes critical in debris-flow prone regions such as Italy,
38 Japan, Hong Kong and earthquake-affected areas in Sichuan, China.

39 During a storm, debris flows may be initiated by surface erosion, slope failures or dam
40 breaching (e.g. Takahashi, 2007), and enlarged during the subsequent flowing process (e.g.
41 Iverson, 1997). The debris flow mixture finally deposits in a flatter area, while the interstice
42 fluid still flows along the debris flow track without further material entrainment as rainfall
43 continues. The evolution of the flowing mixture includes three phases in terms of sediment
44 concentration: clear water flow, hyperconcentrated flow and debris flow. The transition of the
45 flowing mixture between any two phases occurs spatially and temporally during the whole
46 process of rainfall.

47 Many numerical programs have been successfully developed for debris flow analysis,
48 such as DAMBRK (Boss Corporation 1989), FLO-2D (O'Brien et al. 1993), DAN (Hung
49 1995), DMM (Kwan and Sun 2006), Debris2D (Liu and Huang 2006), FLATModel (Medina
50 et al. 2008), MassMov2D (Beguiría et al. 2009), DAN3D (Hung and McDougall 2009),
51 PASTOR (Pastor et al. 2009), RAMMS (Bartelt et al., 2013), EDDA 1.0 (Chen and Zhang
52 2015), DebrisInterMixing (Boetticher et al., 2016) and AschFlow (Quan Luna et al., 2016).
53 These programs can simulate the debris-flow movement with either constant or varying
54 properties of the flowing mixture. The entrainment and deposition processes can also be
55 considered, such as in EDDA 1.0 (Chen and Zhang, 2015).

56 Until now, numerical simulation of the physical process of debris flow initiation is

57 largely avoided in the literature. Moreover, very limited attempt has been made to simulate,
58 in an integrated manner, the entire process from the initiation to the subsequent debris-flow
59 motion and deposition. We address these two research gaps in this paper.

60 Experimental studies and field monitoring have been conducted to study the initiation
61 mechanics of rain-induced debris flows (e.g. Johnson and Sitar, 1990; Cui, 1992; Cannon et
62 al., 2001). A few physical models have been proposed (e.g. Takahashi, 1981; Iverson et al.,
63 1997) to reveal the mechanisms of initiation using infinite slope stability models which are
64 mathematically one-dimensional and statically determinate, leading to unambiguous
65 quantitative results. However, these models do not simulate the debris-flow initiation process,
66 particularly the transformation from a slope failure to a debris flow. Statistical models have
67 also been proposed to relate debris-flow initiation to rainfall (e.g. Caine, 1980; Wieczorek,
68 1987; Chen et al., 2005; Godt et al., 2006; Cannon et al., 2008; Coe et al., 2008; Guzzetti, et
69 al., 2008; Baum and Godt, 2010; Berti et al., 2012; Staley et al., 2013; Zhou and Tang, 2014;
70 De Luca and Versace, 2017a; De Luca and Versace, 2017b; Gao et al., 2017) and other
71 parameters such as surface runoff discharge (Berti and Simoni, 2005) or clay content (Chen et
72 al., 2010). These models are not physically-based.

73 Many of the existing computer programs do not simulate the initiation of debris flows.
74 Instead, they require a predefined empirical hydrograph, created based on the estimated
75 volumes of rainfall runoff and source materials, to initiate a debris flow, which is so called
76 “two-step” analysis (Fig. 1). The “two-step” analysis leads to large uncertainties in debris
77 flow initiation locations, times and volumes when applied to regional debris flow analysis.
78 For instance, Shen et al. (2017) simulated hillslope debris flows initiated from surface
79 erosion, in which the initiation location is artificially intervened (Fig. 1), and the slope failure
80 mechanisms is not included. The integrated simulation of the whole process of the debris
81 flow (Fig. 1) remains an open challenge. In addition, the physical rainfall runoff and overland

82 flow process before the initiation of debris flows is overlooked. Until now, the study on the
83 full evolution in time and space of the flowing mixture is limited.

84 Numerical tools have been generally developed for simulating a single type of hazards.
85 However, multiple types of hazards may be induced by a rainstorm (i.e. slope failures, debris
86 flows and flooding) (e.g. Zhang et al., 2014). One hazard can be the cause of another (e.g.
87 rainfall triggers slope failures that in turn trigger debris flows). Different types of hazards can
88 also interact among each other (e.g. several small debris flows from sub-channels can merger
89 into a larger one). Hazard risk assessment requires hydrological, landslide and debris flow
90 analyses at a regional scale (e.g. Formetta et al., 2011; Archfield et al., 2013). The simulation
91 of the complete processes of possible hazards and their interactions at a regional scale can be
92 a powerful tool to help identify likely hazards, their potentially affected areas and elements at
93 risk. However, the ability of numerical analysis of hazard interactions is still limited (e.g.
94 Kappes et al., 2012; Marzocchi et al., 2012). Using the existing “two-step” tools (Fig. 1) to
95 analyze potential regional hazards could be challenging, since it involves tremendous
96 uncertainties and is time-consuming to conduct the “two-step” analyses for each of all
97 potential hazard locations (e.g. Chen and Zhang, 2015; Gao et al., 2016; Shen et al, 2017).
98 Hence the development of an integrated model for simulating multi-hazard processes and
99 interactions (Fig. 1) is of great theoretical and practical importance.

100 The objectives of this paper are (1) to incorporate debris-flow initiation physically into
101 the debris-flow motion simulation to enable the simulation of the whole process of
102 rain-induced debris flows, (2) to study the full evolution of the flowing mixture in time and
103 space during the whole process of rainfall, and (3) to develop a tool to simulate multi-hazard
104 processes and analyze hazard interactions.

105

106 **2 Methodology**

107 **2.1 Strategy of modeling initiation, dynamics and deposition of debris flows**

108 Intense rainfall in mountainous regions could trigger debris flows from loose soil
109 deposits on hill slopes or in channels. A conceptual model for rain-induced debris flows and
110 likely initiation mechanisms are shown in Fig. 2. Debris flows can be initiated by three
111 mechanisms: transformation from landslides, surface erosion and dam breaching. Due to
112 rainfall infiltration, the hill slope gradually becomes saturated, and the soil loses its strength,
113 causing shallow seated slope failures (Zhang et al., 2011). During a rainstorm, slope failures
114 can occur at different times in space within a catchment. Some of the detached material may
115 move into channels and form landslide dams, and some may transform into debris flows
116 directly. As the surface runoff accumulates, the landslide dam formed earlier in the channel
117 may break, initiating a channelized debris flow (e.g. Liu et al., 2009; Chen et al., 2012; Peng
118 and Zhang, 2012). At the same time, the surface runoff may cause bed erosion and initiate
119 hillslope debris flows (e.g. Cannon et al., 2001). Some of the separate debris flows may
120 merge in the main channel of the drainage basin, forming a larger catastrophic debris flow
121 event (e.g. Iverson et al., 1997). The final magnitude of a debris flow could be many times of
122 its initial volume due to entrainment of materials along the path from additional slope
123 failures, bed erosion or bank collapses (e.g. Iverson et al., 2011; Chen et al., 2012; Ouyang et
124 al., 2015). If reaching a flat residential area downstream the basin, the developed debris flow
125 can cause severe loss of lives and properties.

126 Based on the conceptual model for the whole process of debris flow in Fig. 2, the
127 strategy of the integrated model, including two debris-flow initiation mechanisms (i.e. bed
128 erosion and transformation from landslides) is shown in Fig. 3. The integrated model consists
129 of a digital terrain module, a rainfall module, an infiltration module, an overland flow
130 module, a slope stability module, a surface erosion module, a debris flow dynamics module
131 and a deposition module. The digital terrain module discretizes the study area into a grid

132 system with geological, hydrological and geotechnical information for each cell assigned. All
 133 the computations are based on the concept of cell. As the primary triggering factor, rainfall is
 134 simulated in the rainfall module. Then water infiltration into the ground is simulated to
 135 analyze the pore water pressure profile and compute the surface runoff. The slope stability
 136 and surface erosion are then evaluated in the slope stability module and surface erosion
 137 module, respectively. Once debris flows are initiated by the two physical mechanisms, the
 138 motion of the flowing mixture is analyzed through the debris flow dynamics module.
 139 Material entrainment may occur along the flow path, incorporating solid materials from
 140 addition slope failures and surface erosion. Finally, the deposition process is assessed through
 141 the deposition module. The runout distance, inundation area and deposition volume of the
 142 debris flows can all be assessed.

143

144 **2.2 Debris flow dynamics**

145 The core of the proposed integrated analysis is the debris-flow dynamics simulation and
 146 constitutive modelling of the flowing mixture. The governing equations for debris flow
 147 dynamics describe the mixture movement and changes in debris flow properties, which are
 148 depth-integrated mass conservation equations (Equations 1 and 2) and momentum
 149 conservation equations (Equations 3) (Chen and Zhang, 2015):

$$150 \quad \frac{\partial h}{\partial t} + \frac{\partial(hv)}{\partial x} = i[C_{v^*} + (1 - C_{v^*})s_b] + A[C_{vA} + (1 - C_{vA})s_A] \quad (1)$$

$$151 \quad \frac{\partial(C_v h)}{\partial t} + \frac{\partial(C_v hv)}{\partial x} + = iC_{v^*} + AC_{vA} \quad (2)$$

$$152 \quad \frac{\partial v}{\partial t} + v \frac{\partial v}{\partial x} = g \left[-\text{sgn}(v)S_f - \frac{\partial(z_b + h)}{\partial x} \right] - \frac{v\{i[C_{v^*} + (1 - C_{v^*})s_b] + A[C_{vA} + (1 - C_{vA})s_A]\}}{h} \quad (3)$$

153 where h is the flow depth; v is the depth-integrated flow velocity (m/s); i is the erosion rate (>

154 0) or deposition rate (< 0) (m/s); A is the rate of material entrainment from detached landslide
155 materials (m/s); C_v is the volume fraction of solids in the flowing mixture; C_{v*} and C_{vA} are the
156 volume fraction in the erodible bed and in the entrained materials, respectively; s_b and s_A are
157 the degree of saturation of solids in the erodible bed and in the entrained materials,
158 respectively; S_f is the energy slope; z_b is the bed elevation (m); and the sgn (i.e. signum)
159 function is used to ensure that the direction of the flow resistance is opposite to that of the
160 flow direction.

161 One of the requirements of the integrated analysis is modeling different flowing mixtures
162 simultaneously. The flowing mixture can be classified into three types: clear water flow,
163 hyperconcentrated flow, and fully developed debris flow based on sediment concentration,
164 combining grain-size distribution and particle densities (Pierson, 2005). In this study, the
165 flowing types of mixtures are classified using the volumetric solid concentration C_v ,
166 following FLO-2D Software Inc. (2009):

167 (1) If $C_v < 0.2$, the fluid mixture is deemed clear water flow which has a negligible yield
168 stress and a dynamic viscosity like that of water;

169 (2) If $0.2 < C_v < 0.45$, a hyperconcentrated flow develops with a certain level of
170 increased yield stress and dynamic viscosity;

171 (3) If $0.45 < C_v < 0.6$, the flowing mixture becomes a full debris flow with substantially
172 increased yield stress and dynamic viscosity.

173 Therefore, a proper rheological model must involve C_v to account for the changing
174 properties of the flowing mixture. We adopt different rheological models for different ranges
175 of C_v to deal with this problem. For clear water flow of which C_v is less than 0.2, the energy
176 slope S_f is based on Manning's equation. If $C_v > 0.2$, a quadratic rheological model developed
177 by O'Brien et al. (1993) is used:

178
$$S_f = \frac{\tau_y}{\rho gh} + \frac{K\mu V}{8\rho gh^2} + \frac{n_{td}^2 V^2}{h^{4/3}} \quad (4)$$

179 where ρ is the mass density of the flowing mixture (kg/m^3); τ_y , μ and n_{td} are the yield stress
 180 (Pa), dynamic viscosity (Pa·s) and the equivalent Manning coefficient of the mixture,
 181 respectively; K is the laminar flow resistance. n_{td} is expressed as (FLO-2D Software Inc.,
 182 2009):

183
$$n_{td} = 0.0538ne^{6.0896C_v} \quad (5)$$

184 where n is the Manning coefficient. The following empirical relationships are adopted to
 185 estimate τ_y and μ (O'Brien and Julien, 1988):

186
$$\tau_y = \alpha_1 e^{\beta_1 C_v} \quad (6)$$

187
$$\mu = \alpha_2 e^{\beta_2 C_v} \quad (7)$$

188 where α_1 , α_2 , β_1 , and β_2 are empirical coefficients.

189

190 **2.3 Rainfall infiltration and convolution**

191 Under heavy rainfall, the excess xrainwater will become surface runoff when rainfall
 192 intensity exceeds the infiltration capacity. In EDDA 2.0, the infiltration capacity is assumed
 193 to be the saturated permeability of the surface soil. The surface runoff process is simulated by
 194 solving the governing equations (Eqs. 1-3) and Manning's equation with i , A and C_v equal to
 195 zero. The runoff water may cause surface erosion, or mix with landslide mass or flowing
 196 mixture, which will be described later.

197 Water infiltration will increase the subsurface pore water pressure, causing slope failures
 198 that are normally shallow-seated. The infiltration process is simulated in EDDA 2.0 by
 199 solving the Richards equation with a forward-time central-difference numerical solution.
 200 Non-uniform grid is created along the soil depth to enhance the accuracy of the solution near
 201 boundaries and interfaces. The integrated program calculates the instant pore water pressure

202 profile to facilitate evaluating the slope stability of each cell at each time step.

203

204

205 **2.4 Initiation of debris flows from slope failures**

206 A debris flow may be initiated by transformation from a mass flow of slope failure
207 material at any location and at any time during a storm. The possible locations and
208 approximate failing time can be identified in a cell-based slope stability analysis, if the
209 topography, geology, soil properties etc. are defined properly. To consider this initiation
210 mechanism, the slope instability evaluation must be performed over all the computational
211 cells at each time step.

212 With the knowledge of real-time pore water pressure profiles provided by the infiltration
213 module, a real-time slope instability analysis can follow. Considering that these rain-induced
214 slope failures are shallow-seated, the thickness of the failure mass is small compared to the
215 large plan dimensions of these slopes. Therefore, an infinite slope model for two-layer soil
216 slopes is a reasonable option to evaluate the factor of safety (F_s) (Wu et al., 2016). Following
217 Chen and Zhang (2014), the search for the minimum F_s goes from the ground surface to the
218 wetting front where the volumetric water content changes significantly. If the minimum F_s is
219 smaller than 1, slope failure will occur at the depth corresponding to the minimum F_s . The
220 landslide mass is assumed to be a free-flowing mixture immediately after the slope failure,
221 with a pre-defined C_v value for the soil deposit and a flow depth the same as the failure depth.

222

223 **2.5 Initiation of debris flows due to bed erosion**

224 Intense rainfall can generate plentiful surface runoff, and the soil bed will erode in the
225 runoff water. The initially clear overland flow can gradually develop into a hyperconcentrated
226 flow and finally into a hillslope debris flow, as its C_v value increases through entrainment

227 from bed erosion. To consider this initiation mechanism, the erosion process is analyzed
228 within each computational cell at each time step.

229 We consider the occurrence of erosion under the condition that the bed shear stress is
230 equal or larger than the critical erosive shear stress of the bed material and the volumetric
231 sediment concentration is smaller than an equilibrium value. The equilibrium value proposed
232 by Takahashi et al. (1992) is adopted in this study:

$$233 \quad C_{v\infty} = \frac{\rho_w \tan \theta}{(\rho_s - \rho_w)(\tan \phi_{bed} - \tan \theta)} \quad (8)$$

234 where ϕ_{bed} is the internal friction angle of the erodible bed; ρ_s is the density of soil particles
235 (kg/m^3); ρ_w is the density of water (kg/m^3); and θ is the slope angle.

236 Many researchers have studied the relationship between the soil erosion rate and shear
237 stress. A form of exponential expression has been used for bed erosion in the literature (e.g.
238 Roberts et al., 1998; Chen et al., 2015). More widely used is a linear function of shear stress
239 (e.g. Graf, 1984; Hanson and Simon, 2001; Julian and Torres, 2006; Chang et al., 2011; Chen
240 and Zhang, 2015):

$$241 \quad i = K_e (\tau - \tau_c) \quad (9)$$

242 where i is the erosion rate (m/s); τ is the shear stress at the soil-water interface (Pa); K_e is the
243 coefficient of erodibility ($\text{m}^3/\text{N}\cdot\text{s}$); τ_c is the critical erosive shear stress at the initiation of bed
244 erosion (Pa). The latter two parameters describe the erosion resistance of the bed soil and are
245 related to soil index properties (e.g. Chang et al., 2011; Zhu and Zhang, 2016). The shear
246 stress acting on the bed can be expressed as (e.g. Graf, 1984):

$$247 \quad \tau = \rho g h S_f \quad (10)$$

248 where S_f is the energy slope.

249

250 **2.6 Material exchange: entrainment and deposition**

251 Material exchange occurs as debris flow marches along its flowing path, including
252 material entrainment (solid mass gain from outside of the flowing mixture) and deposition
253 (solid mass loss from inside of the flowing mixture).

254 The entrainment from additional bed erosion or slope failure materials along its
255 trajectory plays a significant role in debris flow volume amplification. The final volume of
256 the debris flow deposit could be many folds of its initial volume. An excellent example is the
257 1990 Tsing Shan debris flow that was the largest ever observed in Hong Kong. An originally
258 small slip of 350 m³ developed into a final volume of 20,000 m³ by entraining colluvium
259 along its flow path (King, 1996). In the integrated model, the landslide mass and surface
260 erosion are considered as the sources of material entrainment. The slope stability and surface
261 erosion evaluation module will be called for every computational cell at every time step;
262 hence the entrainment process is automatically considered once the two modules are called.

263 After flowing into a flatter area, deposition of some solid material will occur. Deposition
264 is deemed to occur if the flow velocity is smaller than a critical value and C_v is larger than the
265 equilibrium value described in Eq. 8. The deposition rate can be expressed as

$$266 \quad i = \delta_d \left(1 - \frac{V}{pV_e} \right) \frac{C_{v\infty} - C_v}{C_{v*}} V \quad (11)$$

267 where V_e is the critical flow velocity following Takahashi et al. (1992); δ_d is a coefficient of
268 deposition rate; p (< 1) is a coefficient accounting for the location difference, and a value of
269 0.67 is recommended (Takahashi et al., 1992); V is the flow velocity; C_{v*} is the volume
270 fraction of solids in the erodible bed. The deposition condition is also detailed in Chen and
271 Zhang (2015).

272

273 **2.7 Numerical scheme**

274 The terrain is discretized into a grid of cells. Each cell is assigned with the input data,

275 including topography, soil depth, geotechnical soil properties, rheological model parameters
276 etc. There are eight flow directions in each cell: four compass directions and four diagonal
277 directions. In each time step, the infiltration is evaluated first to compute the surface runoff
278 and slope stability at each cell. Then changes in flow depth h and volumetric sediment
279 concentration C_v within each cell are evaluated considering the surface runoff, slope failure
280 mass entrainment, erosion, and deposition, followed by computing the flow velocity,
281 discharge and density along the eight flow directions of all the cells, with the averaged
282 surface roughness and slope between two cells computed. The changes in h and C_v due to the
283 flow exchange are evaluated finally at each cell.

284 After all the computations have been completed in each time step, numerical stability
285 criteria are checked for each cell to limit the time step to avoid surging while allowing for
286 large time steps. Three convergence criteria are adopted:

287 (1) The Courant-Friedrichs-Lewy (CFL) condition, with the physical interpretation that a
288 particle of fluid should not travel more than the cell size in one time step (Fletcher,
289 1990), is mostly used in explicit schemes. The time step is limited by

$$290 \quad \Delta t \leq C\Delta x / (\beta V + c) \quad (12)$$

291 where C is the Courant number (C is not smaller than or equal to 1); m is a coefficient
292 ($5/3$ for a wide channel); c is the computed wave celerity.

293 (2) The percent change of flow depth in one time step should not exceed a specified
294 tolerant value, $TOLP(h)$;

295 (3) The change in flow depth in one time step should not exceed a specified tolerant
296 value, $TOL(h)$, which is applied when the flow moves to a cell with zero flow depth.

297 Adjusting these three criteria, the computational time and accuracy could reach a good
298 balance. If all the numerical stability criteria are successfully satisfied, the time step can be
299 increased for the next computational cycle. Otherwise the time step will be reduced and the

300 computation restarted. The volume conservation is computed at the end of each time step for
301 the inflow, outflow, grid system storage and infiltration loss.

302

303 **3 Model verification**

304 The previous version, EDDA 1.0 (Chen and Zhang, 2015), has passed several
305 verification tests including debris flow dynamics, erosion and deposition. In this new version
306 of integrated analysis, the new modules for surface runoff, coupled infiltration and slope
307 stability analysis, and the integrated program require further verification. The response of
308 Xiaojiagou Ravine during a rainstorm in August 2010 is used to verify the new modules. The
309 in-situ conditions shortly after the 2010 Xiaojiagou debris flow event are shown in Fig. 4.
310 The Xiaojiagou Ravine has an area of 7.84 km². The elevation of the ravine ranges between
311 1,100 m and 3,200 m. The hill slopes within the ravine are very steep with an average slope
312 angle of 46°. There are one main drainage channel and four branches within the Xiaojiagou
313 Ravine. The loose soil deposits on the hill slopes and channels of the ravine before the debris
314 flow event are identified based on field investigations and interpretation of satellite image
315 (e.g. Chen and Zhang, 2014). The rainstorm process triggering the catastrophic Xiaojiagou
316 debris flow is presented in Fig. 5. The rainstorm lasted about 40 hours with a total
317 precipitation of 220 mm.

318 First the performance of the rainfall-runoff module of the integrated program is
319 compared with a commonly used program FLO-2D (FLO-2D Software Inc., 2009). Then, the
320 infiltration module is checked against an analytical solution under steady rainfall. The slope
321 stability analysis is verified by comparing with the landslide satellite image and the
322 computation results by Chen and Zhang (2014). Finally, the performance of the integrated
323 model is checked against the 2010 Xiaojiagou debris flow event in Section 4.

324

325 **3.1 Verification test 1: rainfall runoff**

326 The same input data are used in EDDA 2.0 and FLO-2D, including the digital elevation
327 model, Manning's coefficient ($n = 0.3$), the limiting Froude number ($L_f = 0.8$), the saturated
328 permeability of the surface soil ($k_{st} = 3.6 \text{ mm/h}$ or 10^{-6} m/s) and the rainfall data (Fig. 5).
329 Other hydrological parameters such as the soil porosities used in FLO-2D are adopted
330 following Chen et al. (2013) and Shen et al. (2017).

331 The results from the two programs are compared in Fig. 6, including the distributions of
332 the maximum flow depth and flow velocity. The result from FLO-2D (Figs. 6a and 6c) differ
333 only slightly from those of EDDA 2.0 (Figs. 6b and 6d). During the rainstorm process, the
334 maximum flow depth computed by FLO-2D is 3.2 m, while that by EDDA 2.0 is 3.4 m. The
335 outflow hydrographs recorded at the mouth of the ravine of the two programs are shown in
336 Fig. 7. The computed overall discharge processes from both programs are very close.

337

338 **3.2 Verification test 2: infiltration process and resulting pore-water pressure changes**

339 Before applying the infiltration module to compute the pore water pressure profiles
340 under the actual rainfall event, four cases of infiltration under steady rainfall are adopted to
341 verify the infiltration module. The results are compared with those from an analytical solution
342 by Srivastava and Yeh (1991) and Zhan et al. (2013). The scenario of two-layer soil is
343 considered, which is also used in the field application. Table 1 presents the input parameters
344 for the four cases. Four combinations are set up to represent likely in-situ conditions. The
345 results from the numerical infiltration module and the analytical solution are compared in Fig.
346 8. For all the four cases, the module performance is satisfactory.

347

348 **3.3 Verification test 3: slope stability analysis**

349 The 2008 Wenchuan earthquake triggered over 50,000 landslides within the earthquake

350 region, leaving a large amount of loose materials on hill slopes and in channels (Fig. 4).
351 These materials became the source of numerous post-earthquake rain-induced landslides and
352 debris flows. Until now, nearly 80% of such materials remained in the mountain regions,
353 posing great potential threats (Zhang et al., 2016). EDDA 2.0 is used to reproduce the slope
354 failures under the rainstorm in August 2010 (Fig. 5) by Chen and Zhang (2014), who
355 evaluated the slope stability of a 164.5 km² area near the epicenter. All the parameters are the
356 same as those in that study, with the only difference being that the area concerned in this
357 study is only Xiaojiagou Ravine (Fig. 4). The loose soil deposits are assumed to be two
358 layers. Given the same parameters such as the topography, layer thicknesses and soil
359 properties, the unstable cells when rainfall terminates are computed using the slope failure
360 module. Comparing the simulation results with the observation (Fig. 9), the computed
361 unstable cells generally fall upon the landslide scars formed during the rainstorm event.
362 Moreover, the results are compared with those by Chen and Zhang (2014), which have been
363 verified using the confusing matrix method (e.g. Van Den Eeckhaut et al., 2006). It is found
364 that the results of the two separate analyses are very similar. The computed total scar area is
365 $4.42 \times 10^5 \text{ m}^2$, comparing well with $5.20 \times 10^5 \text{ m}^2$ from the satellite image. The difference is
366 15%. It is concluded that the proposed slope stability module performs reasonably well.

367

368 **4 Field application**

369 **4.1 Xiaojiagou debris flow on 14 August 2010**

370 A heavy rainstorm swept the epicenter, Yinxiu town, and its vicinity. The rainstorm
371 lasted about 40 h from 12 to 14 August 2010, pouring about 220 mm of precipitation in total
372 (Fig. 5). A catastrophic debris flow was triggered by the storm in Xiaojiagou Ravine (Fig. 4).
373 The debris flow was witnessed at the ravine mouth at about 5:00 am on 14 August and lasted
374 about 30 min. About $1.17 \times 10^6 \text{ m}^3$ of the soil deposit was brought out of the Xiaojiagou

375 Ravine mouth in a form of a channelized debris flow. The runout material deposited in front
376 of the mouth, burying 1100 m of Province Road 303 (PR303), blocking Yuzixi River, forming
377 a debris flow barrier and raising the river bed by at least 15 m.

378

379 **4.2 Input information**

380 In EDDA 1.0, the study area has to be divided into two domains for rainfall runoff
381 simulation and debris-flow runout simulation respectively. However, in the integrated
382 simulation by EDDA 2.0, only one grid of 9500 cells 30×30 m in size is created (Fig. 2).
383 After the Xiaojiagou debris flow, detailed field investigations and laboratory tests were
384 conducted (Chen et al., 2012), as well as numerical back analysis (Chen et al., 2013). The
385 study area is divided into four zones by satellite interpretation: bare soil, vegetated soil, bed
386 rock and river bed (Chen and Zhang, 2014). The soil properties of each zone and the
387 constitutive (or rheological) parameters used in the integrated simulation are determined
388 following EDDA 1.0 (Chen and Zhang, 2015), shown in Tables 2-4. The erosion resistance
389 parameters τ_c and K_e of the soils are determined using the empirical equations based on field
390 tests in the Wenchuan earthquake zone (Chang et al., 2011):

$$391 \quad \tau_c = 6.8PI^{1.68}P^{-1.73}e^{-0.97} \quad (13)$$

$$392 \quad K_e = 0.020075e^{4.77}C_u^{-0.76} \quad (14)$$

393 where e is the void ratio; PI is the plasticity index; P is the fines content (< 0.063 mm); C_u is
394 the coefficient of uniformity. These four soil properties are determined to be 1.05, 18, 14 and
395 2000, respectively, according to Chang et al. (2011). Therefore, τ_c and K_e are estimated to be
396 8.7 Pa and 7.8×10^{-8} m³/N-s, respectively.

397

398 **4.3 Integrated simulation results**

399 We examine the final output of the integrated simulation first. Erosion plays an

400 important role in the volume magnification of debris flows. The final erosion depths in the
401 eroded areas are shown in Fig. 10a. The most eroded areas during the Xiaojiagou debris flow
402 event were in channels, where a huge amount of loose solid material was present (Chen et al.,
403 2012). Loose deposits on the hill slopes also eroded after the landslide bodies detached from
404 their original locations and slid down the slopes. The distribution of the eroded areas reflects
405 that the debris flows were initiated from both slope failures and surface erosion, then
406 developed along the channels by further erosion and entrainment of the slope failure
407 materials, which are the two mechanisms considered in the integrated model. The distribution
408 of the maximum flow velocity is shown in Fig. 10b, with the maximum value being 9.5 m/s,
409 which is very close to that from EDDA 1.0 (9.1 m/s). The slightly larger value of flow
410 velocity from EDDA 2.0 is attributed to the consideration of the extra surface runoff within
411 domain two created when using EDDA 1.0 (Fig. 2). The maximum velocity occurs in the
412 ravine channels, indicating that the debris flow moves very rapidly.

413 The simulated and observed deposition areas are compared in Fig. 11. It is seen that the
414 simulation results (Fig. 11a) match the observation (Fig. 11b) reasonably well. The simulated
415 deposition depth is approximately 20 m, very close to that of the observed thickness of the
416 deposit fan during the field investigations. The total volume of the observed deposition fan is
417 about $1.17 \times 10^6 \text{ m}^3$, while the simulated deposition volume of the debris flow is 0.9×10^6
418 m^3 . The integrated model evaluates a smaller debris flow volume and the difference is about
419 23%. The main uncertainty arises from the slope failure module and surface erosion module.

420 The changes in the volumetric sediment concentration C_v and the discharge hydrograph
421 at Section 1-1 (Fig. 4) are recorded during the simulation of the whole rainfall process, shown
422 in Fig. 12. The integrated model simulates two peaks in the discharge process throughout the
423 rainfall with a precursory boulder front arriving in advance. At around 12 h, the value of C_v
424 increases very quickly to a peak value of 0.6, indicating the arrival of the debris flow.

425 Afterwards, C_v decreases, which can be viewed as a hyperconcentrated flow or a clear water
426 flow after the debris flow passes. Another large debris flow surge is simulated at around 32 h
427 with the same pattern as the first one. The debris flow passes through Section 1-1 (Fig. 4)
428 first and continues to develop for some time. After most of the solid materials are brought
429 away by the debris flow surge, the flow at Section 1-1 becomes a hyperconcentrated flow,
430 and the flowing mixture gradually becomes a clear water flow as the rainwater continues to
431 generate surface runoff without further material entrainment. The integrated simulation is
432 capable of simulating multiple debris flow surges and the changes in the flowing mixture
433 properties throughout a rainfall event.

434 To demonstrate the evolution of the flowing mixture within the drainage basin, the
435 distributions of C_v at four snapshots during the storm are shown in Fig. 13. The recording
436 times of these four figures span a complete evolution cycle, i.e. clear water flow (Fig. 13a),
437 debris flow initiation (Fig. 13b), debris flow motion (Fig. 13c), and hyperconcentrated
438 flow/clear water flow (Fig. 13d). This evolution cycle could occur within the basin several
439 times in different branch channels, which can be captured by the integrated model.

440

441 **5 Limitations of EDDA 2.0**

442 We have successfully extended the “two-step” debris-flow simulation to an integrated
443 simulation of the whole process of rain-induced debris flows. However, there are still
444 limitations in the underlying assumptions and simplifications:

- 445 1. EDDA 2.0 considers the initiation of debris flows from transformation of slope
446 failures and surface erosion. However, the initiation from dam breaching has not yet
447 been tested.
- 448 2. The studies consider material entrainment from surface erosion and slope failure
449 detachment, but the entrainment from bank failures can only be considered using an

450 empirical rate, instead of through a three-dimensional physical model.

451 3. The governing equations are in a depth-integrated form; hence particle segregation
452 in the vertical direction cannot be considered.

453 4. The rheological models for the hyperconcentrated flow, fully developed debris flow
454 and slope failure mass flow need further study. Particularly, the slope failure mass
455 movement is critical for estimating the transformation rate from a slope failure to a
456 debris flow.

457

458 **6 Summary and conclusions**

459 A new integrated simulation model is developed for simulating rain-induced debris-flow
460 initiation, motion, entrainment, deposition and property changes. The model is unique in that
461 it simulates the whole process of rain-induced debris flow evolution and two physical
462 initiation mechanisms (i.e. transformation from landslides and surface erosion). Previous
463 “two-step analysis” with an assumed inflow hydrograph and an inflow location can now be
464 conducted at one go scientifically without subjective assumptions.

465 Three numerical tests have been conducted to verify the performance of the newly added
466 modules of the integrated model. The Xiaojiagou Ravine landslides and debris flows
467 triggered by the rainstorm in August 2010 were used as a verification case. In test 1, the
468 rainfall runoff simulation by EDDA 2.0 was compared to FLO-2D. The simulation results
469 from the two models are very close, which indicates that EDDA 2.0 simulates rainfall runoff
470 well. In test 2, an analytical solution for evaluating pore water pressure profile under
471 infiltration is adopted. Comparison between the model solution and the analytical solution
472 indicates that the integrated model evaluates the infiltration process well. The regional slope
473 stability within the study area under the same rainstorm was evaluated using the integrated
474 model in test 3. The computed unstable cells compare well with the observations from

475 satellite images and the results from previous studies.

476 The new integrated model was finally applied to reproduce the Xiaojiagou debris flow
477 event. The model can simulate the entire evolution process of rain-induced debris flows, and
478 estimates reasonably well the volume, inundated area and runout distance of the debris flow.
479 It is concluded that the new integrated debris flow simulation model, EDDA 2.0, is capable of
480 (1) simulating the whole process of rain-induced debris flow from debris-flow initiation to
481 post-initiation debris-flow motion, entrainment and deposition, and (2) tracing the evolution
482 of the flowing mixture in time and space during the whole process of rainfall. The integrated
483 model will serve as a powerful tool for analyzing multi-hazard processes and hazard
484 interactions, and assessment of regional debris-flow risks in the future.

485

486 ***Code availability.*** EDDA 2.0 is written in FORTRAN, which can be compiled using Intel
487 FORTRAN Compilers. A doi has been generated for the source code and the source code is
488 available online at <http://doi.org/10.5281/zenodo.1033377>. The source code is also available
489 online as a supplementary material to this paper. The main subroutine is “dfs.F90”, which
490 presents the numerical solution algorithm for evaluating debris flow initiation from erosion
491 and slope failures, and for solving the governing equations of the dynamics of the flowing
492 mixture. An input file is needed (“edda_in.txt”) for inputting material properties, hydrological
493 and rheological parameters and control settings. As an integrated program, EDDA 2.0 can be
494 used to analyse regional slope failures, so the “edda_in.txt” file also includes the material
495 properties and controlling options for slope stability analysis. Another input file
496 (“outflow.txt”) is required to define the outflow cell. Digital terrain data (e.g. surface
497 elevation, slope gradient and erodible layer thickness) are included in separate ASCII grid
498 files and enclosed in the data folder. Output files are stored in the results folder and output
499 variables at selected points are stored in “EDDA_Log.txt”.

500

501 **Author contributions.** Limin Zhang and Ping Shen conceived the methodology and
502 formulated the model. Ping Shen programmed the analysis code and performed the analysis.
503 Hongxin Chen and Ruilin Fan evaluated the model results. All authors contributed to the
504 writing of the manuscript.

505

506 **Competing interests.** The authors declare that they have no conflict of interest.

507

508 **Acknowledgements.** The authors acknowledge the support from the Research Grants Council
509 of the Hong Kong SAR (No. C6012-15G and No. 16206217).

510

511 **References**

512 Archfield, S. A., Steeves, P. A., Guthrie, J. D., and Ries III, K. G.: Towards a publicly
513 available, map-based regional software tool to estimate unregulated daily streamflow at
514 ungauged rivers, *Geosci. Model Dev.*, 6, 101-115, doi:10.5194/gmd-6-101-2013, 2013.

515 Baum, R. L. and Godt, J. W.: Early warning of rainfall-induced shallow landslides and debris
516 flows in the USA, *Landslides*, 7(3), 259-272, doi: 10.1007/s10346-009-0177-0, 2010.

517 Bartelt, P., Buehler, Y., Christen, M., Deubelbeiss, Y., Graf, C., McArdell, B., Salz, M., and
518 Schneider, M.: A numerical model for debris flow in research and practice, User Manual
519 v1.5 Debris Flow, WSL Institute for Snow and Avalanche Research SLF, Switzerland,
520 2013.

521 Beguería, S., Van Asch, Th. W. J., Malet, J.-P., and Gröndahl, S.: A GIS-based numerical
522 model for simulating the kinematics of mud and debris flows over complex terrain, *Nat.*
523 *Hazard Earth Sys.*, 9, 1897-1909, doi:10.5194/nhess-9-1897-2009, 2009.

524 Berti, M. and Simoni, A.: Experimental evidences and numerical modelling of debris flow

525 initiated by channel runoff, *Landslides*, 2, 171-182, doi:10.1007/s10346-005-0062-4,
526 2005.

527 Berti, M., Martina, M. L. V., Franceschini, S., Pignone, S., Simoni, A., and Pizziolo, M.:
528 Probabilistic rainfall thresholds for landslide occurrence using a Bayesian approach, *J.*
529 *Geophys. Res-Earth*, 117(4), doi:10.1029/2012JF002367, 2012.

530 Boetticher, A. V., Turowski, J. M., McArdell, B. W., Rickenmann, D., and Kirchner, J. W.:
531 DebrisInterMixing-2.3: a finite volume solver for three-dimensional debris-flow
532 simulations with two calibration parameters - Part 1: Model description, *Geosci. Model*
533 *Dev.*, 9, 2909-2923, doi:10.5194/gmd-9-2909-2016, 2016.

534 Boss Corporation: DAMBRK-User's manual, Boss International Inc., Madison, Wisconsin,
535 USA, 1989.

536 Caine, N.: The rainfall intensity: duration control of shallow landslides and debris flows,
537 *Geogr. Ann. A*, 62, 23-27, doi: 10.2307/520449, 1980.

538 Cannon, S. H., Kirkham, R. M., and Parise, M.: Wildfire-related debris-flow initiation
539 processes, Storm King Mountain, Colorado, *Geomorphology*, 39, 171-188,
540 doi:10.1016/S0169-555X(00)00108-2, 2001.

541 Cannon, S. H., Gartner, J. E., Wilson, R., Bowers, J., and Laber, J.: Storm rainfall conditions
542 for floods and debris flows from recently burned areas in southwestern Colorado and
543 southern California, *Geomorphology*, 96(3-4), 250-269, doi:
544 10.1016/j.geomorph.2007.03.019, 2008.

545 Chang, D. S., Zhang, L. M., Xu, Y., and Huang, R. Q.: Field testing of erodibility of two
546 landslide dams triggered by the 12 May Wenchuan earthquake, *Landslides*, 8, 321-332,
547 doi:10.1007/s10346-011-0256-x, 2011.

548 Chen, C. Y., Chen, T. C., Yu, F. C., Yu, W. H., and Tseng, C. C.: Rainfall duration and
549 debris-flow initiated studies for real-time monitoring, *Environ. Geol.*, 47, 715-724,

550 doi:10.1007/s00254-004-1203-0, 2005.

551 Chen, H. X. and Zhang, L. M.: A physically-based distributed cell model for predicting
552 regional rainfall-induced shallow slope failures, *Eng. Geol.*, 176, 79-92,
553 doi:10.1016/j.enggeo.2014.04.011, 2014.

554 Chen, H. X. and Zhang, L. M.: EDDA 1.0: integrated simulation of debris flow erosion,
555 deposition and property changes, *Geosci. Model Dev.*, 8, 829-844,
556 doi:10.5194/gmd-8-829-2015, 2015.

557 Chen, H. X., Zhang, L. M., Chang, D. S., and Zhang, S.: Mechanisms and runout
558 characteristics of the rainfall-triggered debris flow in Xiaojiagou in Sichuan Province,
559 China, *Nat. Hazards*, 62, 1037-1057, doi:10.1007/s11069-012-0133-5, 2012.

560 Chen, H. X., Zhang, L. M., Zhang, S., Xiang, B., and Wang, X. F.: Hybrid simulation of the
561 initiation and runout characteristics of a catastrophic debris flow, *J. Mt. Sci.*, 10,
562 219-232, doi:10.1007/s11629-013-2505-z, 2013.

563 Chen, N. S., Zhou, W., Yang, C. L., Hu, G. S., Gao, Y. C., and Han, D.: The processes and
564 mechanism of failure and debris flow initiation for gravel soil with different clay
565 content, *Geomorphology*, 121, 222-230, doi:10.1016/j.geomorph.2010.04.017, 2010.

566 Chen, Z., Ma, L., Yu, S., Chen, S., Zhou, X., Sun, P., and Li, X.: Back analysis of the draining
567 process of the Tangjiashan barrier lake, *J. Hydraul Eng.*, 141(4), 05014011, doi:
568 10.1061/(ASCE)HY.1943-7900.0000965, 2015.

569 Coe, J. A., Kinner, D. A., and Godt, J. W.: Initiation conditions for debris flows generated by
570 runoff at Chalk Cliffs, central Colorado, *Geomorphology*, 96, 270-297,
571 doi:10.1016/j.geomorph.2007.03.017, 2008.

572 Cui, P.: Study on condition and mechanisms of debris flow initiation by means of experiment,
573 *Chinese Sci. Bull.*, 37, 759-763, 1992.

574 De Luca D. L. and Versace P. A.: Comprehensive framework for empirical modeling of

575 landslides induced by rainfall: the Generalized FLAIR Model (GFM), *Landslides*, 14(3),
576 1009-1030, ISSN: 1612-5118, DOI: 10.1007/s10346-016-0768-5, 2017a.

577 De Luca, D. L. and Versace, P.: Diversity of Rainfall Thresholds for early warning of
578 hydro-geological disasters, *Adv. Geosci.*, 44, 53-60,
579 <https://doi.org/10.5194/adgeo-44-53-2017>, 2017b.

580 Fletcher, C. A. J.: *Computational Techniques for Fluid Dynamics, Volume I*, 2nd ed.,
581 Springer-Verlag, New York, 1990.

582 FLO-2D Software Inc.: *FLO-2D reference manual*, Nutrioso, Arizona, USA, 2009.

583 Formetta, G., Mantilla, R., Franceschi, S., Antonello, A., and Rigon, R.: The JGrass-NewAge
584 system for forecasting and managing the hydrological budgets at the basin scale: models
585 of flow generation and propagation/routing, *Geosci. Model Dev.*, 4, 943-955,
586 doi:10.5194/gmd-4-943-2011, 2011.

587 Gao, L., Zhang, L. M., Chen, H. X., and Shen, P.: Simulating debris flow mobility in urban
588 settings, *Eng. Geol.*, 214, 67-78, doi:10.1016/j.enggeo.2016.10.001, 2016.

589 Gao, L., Zhang, L. M., and Cheung, R. W. M.: Relationships between natural terrain landslide
590 magnitudes and triggering rainfall based on a large landslide inventory in Hong Kong,
591 *Landslides*, DOI: 10.1007/s10346-017-0904-x, 2017.

592 Godt, J. W., Baum, R. L., and Chleborad, A. F.: Rainfall characteristics for shallow
593 landsliding in Seattle, Washington, USA. *Earth Surf. Proc. Land*, 31, 97-110, doi:
594 10.1002/esp.1237, 2006.

595 Graf, W. H.: *Hydraulics of sediment transport*, Water Resources Publications, Colorado,
596 1984.

597 Guzzetti, F., Peruccacci, S., Rossi, M., and Stark, C. P.: The rainfall intensity-duration control
598 of shallow landslides and debris flows: An update, *Landslides*, 5, 3-17, doi:
599 10.1007/s10346-007-0112-1, 2008.

600 Hanson, G. J. and Simon, A.: Erodibility of cohesive streambeds in the loess area of the
601 midwestern USA, *Hydrolo. Process.*, 15(1), 23-38, doi: 10.1002/hyp.149, 2001.

602 Hungr, O.: A model for the runout analysis of rapid flow slides, debris flows, and avalanches,
603 *Can. Geotech. J.*, 32, 610-623, doi:10.1139/t95-063, 1995.

604 Hungr, O. and McDougall, S.: Two numerical models for landslide dynamic analysis,
605 *Computat. Geosci.*, 35(5), 978-992, doi: 10.1016/j.cageo.2007.12.003, 2009.

606 Iverson, R. M.: The physics of debris flows, *Rev. Geophys.*, 35(3), 245-296, doi:
607 10.1029/97RG00426, 1997.

608 Iverson, R. M., Reid, M. E., and LaHusen, R. G.: Debris-flow mobilization from landslides,
609 *Annu. Rev. Earth Pl. Sc.*, 25(1), 85-138, doi: 10.1146/annurev.earth.25.1.85, 1997.

610 Iverson, R. M., Reid, M. E., Logan, M., LaHusen, R. G., Godt, J. W., and Griswold, J. P.:
611 Positive feedback and momentum growth during debris-flow entrainment of wet bed
612 sediment, *Nat. Geosci.*, 4, 116-121, doi:10.1038/ngeo1040, 2011.

613 Johnson, K. A. and Sitar, N.: Hydrologic conditions leading to debris-flow initiation, *Can.*
614 *Geotech. J.*, 27, 789-801, doi:10.1139/t90-092, 1990.

615 Julian, J. P. and Torres, R.: Hydraulic erosion of cohesive riverbanks, *Geomorphology*,
616 76(1-2), 193-206, doi: 10.1016/j.geomorph.2005.11.003, 2006.

617 Kappes, M. S., Keiler, M., von Elverfeldt, K. and Glade, T.: Challenges of analyzing
618 multi-hazard risk: a review, *Nat. Hazards*, 64(2), 1925-1958, doi:
619 10.1007/s11069-012-0294-2, 2012.

620 King, J.: Tsing Shan debris flow, Special Project Report SPR 6/96, Geotechnical Engineering
621 Office, Hong Kong Government, 133, 1996.

622 Kwan, J. S. and Sun, H.: An improved landslide mobility model, *Can. Geotech. J.*, 43(5),
623 531-539, doi: 10.1139/t06-010, 2006.

624 Lee, B. Y., Mok, H. Y., and Lee, T. C.: The latest on climate change in Hong Kong and its

625 implications for the engineering sector, DHKO in the HKIE Conf. on Climate Change -
626 Hong Kong Engineers' Perspective, Hong Kong Observatory, Government of Hong
627 Kong SAR, Hong Kong, 2010.

628 Liu, K. F. and Huang, M. C.: Numerical simulation of debris flow with application on hazard
629 area mapping, *Computat. Geosci.*, 10, 221-240, doi: 10.1007/s10596-005-9020-4, 2006.

630 Liu, N., Zhang, J. X., Lin, W., Cheng, W. Y., and Chen, Z. Y.: Draining Tangjiashan Barrier
631 Lake after Wenchuan Earthquake and the flood propagation after the dam break, *Sci.*
632 *China Ser. E.*, 52(4), 801–809, doi: 10.1007/s11431-009-0118-0, 2009.

633 Marzocchi, W., Garcia-Aristizabal, A., Gasparini, P., Mastellone, M. L., and Di Ruocco, A.:
634 Basic principles of multi-risk assessment: a case study in Italy, *Nat. Hazards*, 62(2),
635 551-573, doi: 10.1007/s11069-012-0092-x, 2012.

636 Medina, V., Hürlimann, M., and Bateman, A.: Application of FLATModel, a 2-D finite
637 volume code, to debris flows in the northeastern part of the Iberian Peninsula,
638 *Landslides*, 5, 127-142, doi: 10.1007/s10346-007-0102-3, 2008.

639 O'Brien, J. S. and Julien, P. Y.: Laboratory analysis of mudflow properties, *J. Hydraul. Eng.*,
640 114, 877-887, doi: 10.1061/(ASCE)0733-9429(1988)114:8(877), 1988.

641 O'Brien, J. S., Julien, P. Y., Fullerton, W. T.: Two-dimensional water flood and mudflow
642 simulation, *J. Hydraul. Eng.*, 119, 244-261, doi:
643 10.1061/(ASCE)0733-9429(1993)119:2(244), 1993.

644 Ouyang, C., He, S., and Tang, C.: Numerical analysis of dynamics of debris flow over
645 erodible beds in Wenchuan earthquake-induced area, *Eng. Geol.*, 194, 62-72, doi:
646 10.1016/j.enggeo.2014.07.012, 2015.

647 Pastor, M., Haddad, B., Sorbino, G., Cuomo, S., and Drempetic, V.: A depth-integrated,
648 coupled SPH model for flow-like landslides and related phenomena, *Int. J. Numer. Anal.*
649 *Met.*, 33(2), 143-172, doi: 10.1002/nag.705, 2009.

650 Peng, M., and Zhang, L.M.: Breaching parameters of landslide dams, *Landslides*, 9(1): 13–
651 31, doi: 10.1007/s10346-011-0271-y, 2012.

652 Pierson, T. C.: Hyperconcentrated flow - transitional process between water flow and debris
653 flow. In *Debris-flow hazards and related phenomena* (eds. Jakob, M. and Hungr, O.),
654 Springer-Praxis, Chichester, UK, 159-202, doi: 10.1007/3-540-27129-5_8, 2005.

655 Quan Luna, B., Blahut, J., van Asch, T., van Westen, C., and Kappes, M.: ASCHFLOW-A
656 dynamic landslide run-out model for medium scale hazard analysis, *Geoenvironmental*
657 *Disasters*, 3(1), 29, 10.1186/s40677-016-0064-7, 2016.

658 Raia, S., Alvioli, M., Rossi, M., Baum, R. L., Godt, J. W., and Guzzetti, F.: Improving
659 predictive power of physically based rainfall-induced shallow landslide models: a
660 probabilistic approach, *Geosci. Model Dev.*, 7, 495-514, doi:10.5194/gmd-7-495-2014,
661 2014.

662 Roberts, J., Jepsen, R., Gotthard, D., and Lick, W.: Effects of particle size and bulk density on
663 erosion of quartz particles, *J. Hydraul Eng.*, doi:
664 10.1061/(ASCE)0733-9429(1998)124:12(1261), 1261-1267, 1998.

665 Shen, P., Zhang, L. M., Chen, H. X., and Gao, L.: Role of vegetation restoration in mitigating
666 hillslope erosion and debris flows, *Eng. Geol.*, 216, 122-133, doi:
667 10.1016/j.enggeo.2016.11.019, 2017.

668 Srivastava, R. and Yeh, T. C. J.: Analytical solutions for one-dimensional, transient
669 infiltration toward the water table in homogeneous and layered soils, *Water Resour.*
670 *Res.*, 27, 753-762, doi:10.1029/90WR02772, 1991.

671 Staley, D. M., Kean, J. W., Cannon, S. H., Schmidt, K. M., and Laber, J. L.: Objective
672 definition of rainfall intensity–duration thresholds for the initiation of post-fire debris
673 flows in southern California, *Landslides*, 10(5), 547-562, doi:
674 10.1007/s10346-012-0341-9, 2013.

675 Takahashi, T.: Debris flow, *Annu. Rev. Fluid Mech.*, 13, 57-77, 1981.

676 Takahashi, T.: Debris flow: mechanics, prediction and countermeasures, Taylor & Francis,
677 London, UK, 2007.

678 Takahashi, T., Nakagawa, H., Harada, T., and Yamashiki, Y.: Routing debris flows with
679 particle segregation, *J. Hydraul. Eng.*, 118, 1490-1507,
680 doi:10.1061/(ASCE)0733-9429(1992)118:11(1490), 1992.

681 Tang, C., Rengers, N., van Asch, Th.W.J., Yang, Y. H., and Wang, G. F.: Triggering conditions
682 and depositional characteristics of a disastrous debris flow event in Zhouqu city, Gansu
683 Province, northwestern China, *Nat. Hazard Earth Sys.*, 11, 2903-2912,
684 doi:10.5194/nhess-11-2903-2011, 2011.

685 Van Den Eeckhaut, M., Vanwalleghem, T., Poesen, J., Govers, G., Verstraeten, G.,
686 Vandekerckhove, L.: Prediction of landslide susceptibility using rare events logistic
687 regression: a case-study in the Flemish Ardennes (Belgium), *Geomorphology*, 76(3),
688 392-410, doi: 10.1016/j.geomorph.2005.12.003, 2006.

689 Wieczorek, G. F.: Effect of rainfall intensity and duration on debris flows in central Santa
690 Cruz Mountains, California, *Rev. Eng. Geol.*, 7, 93-104, doi:10.1130/REG7-p93, 1987.

691 Wong, H. N.: Rising to the challenges of natural terrain landslides, *Natural Hillside: Study
692 and Risk Management Measures, Proc.*, 29th Annual Seminar of the HKIE Geotechnical
693 Division, Hong Kong Institution of Engineers, Hong Kong, 15-53, 2009.

694 Wu, L. Z., Selvadurai, A. P. S., Zhang, L. M., Huang, R. Q., and Huang, J.: Poro-mechanical
695 coupling influences on potential for rainfall-induced shallow landslides in unsaturated
696 soils, *Adv. Water Resour.*, 98, 114-121, doi: 10.1016/j.advwatres.2016.10.020, 2016.

697 Zhan, T. L., Jia, G. W., Chen, Y. M., Fredlund, D. G., and Li, H.: An analytical solution for
698 rainfall infiltration into an unsaturated infinite slope and its application to slope stability
699 analysis, *Int. J. Numer. Anal. Met.*, 37, 1737-1760, doi:10.1002/nag.2106, 2013.

700 Zhang, L. L., Zhang, J., Zhang, L. M., and Tang, W. H.: Stability analysis of rainfall-induced
701 slope failure: a review, *Proceedings of the ICE-Geotechnical Engineering*, 164, 299,
702 2011.

703 Zhang, L. M., Zhang, S., and Huang, R. Q.: Multi-hazard scenarios and consequences in
704 Beichuan, China: The first five years after the 2008 Wenchuan earthquake, *Engineering*
705 *Geology*, 180, 4-20, 2014.

706 Zhang, S., Zhang, L. M., Chen, H. X., Yuan, Q., and Pan, H.: Changes in runout distances of
707 debris flows over time in the Wenchuan Earthquake zone, *J. Mt. Sci.*, 10, 281-292,
708 doi:10.1007/s11629-012-2506-y, 2013.

709 Zhang, S., Zhang, L. M., Lacasse, S., and Nadim, F.: Evolution of mass movements near
710 epicentre of Wenchuan earthquake, the first eight years. *Sci. Rep.*, 6, 36154, 2016.

711 Zhou, W. and Tang, C.: Rainfall thresholds for debris flow initiation in the Wenchuan
712 earthquake-stricken area, southwestern China, *Landslides*, 11, 877-887,
713 doi:10.1007/s10346-013-0421-5, 2014.

714 Zhu, H., and Zhang, L.M.: Field investigation of erosion resistance of common grass species
715 for soil-bioengineering in Hong Kong, *Acta Geotechnica*, 11(5), 1047–1059, doi:
716 10.1007/s11440-015-0408-6, 2016.

717 **List of Captions**

718

719 **Table captions**

720 **Table 1.** Parameters used in the infiltration module verification.

721 **Table 2.** Properties of four types of superficial materials.

722 **Table 3.** Soil properties for debris flow simulation.

723 **Table 4.** Constitutive (rheological) parameters for debris flow simulation.

724

725 **Figure captions**

726 **Figure 1.** Conceptual model of a rain-induced debris flow and three typical initiation
727 mechanisms of debris flows: bed erosion, transformation from landslide, and dam
728 breach.

729 **Figure 2.** Comparison between “two-step” simulation and integrated simulation of
730 rain-induced debris flows.

731 **Figure 3.** Framework of the integrated simulation of debris flows.

732 **Figure 4.** A satellite image of the study area taken shortly after the Xiaojiagou debris flow on
733 14 August 2010.

734 **Figure 5.** Rainfall process of the August 2010 rainstorm.

735 **Figure 6.** Comparison of the maximum surface runoff flow depths and flow velocities
736 simulated using FLO-2D [(a) and (b)] and EDDA 2.0 [(c) and (d)].

737 **Figure 7.** Comparison of the outflow hydrographs at the ravine mouth using FLO-2D and
738 EDDA 2.0.

739 **Figure 8.** Pore water pressure profiles at various times: (a) Case 1; (b) Case 2; (c) Case 3; (d)
740 Case 4.

741 **Figure 9.** Computed unstable cells vs. landslide scars on the satellite image.

742 **Figure 10.** Simulation results of the Xiaojiagou debris flow: (a) final shape and depth of the
743 erosion zone; (b) maximum flow velocity.

744 **Figure 11.** Comparison of the simulated and observed deposition zones: (a) simulation result;
745 (b) enlarged view of the observed deposition area (Chen and Zhang, 2015).

746 **Figure 12.** Outflow hydrograph and changes in C_v at the Xiaojiagou Ravine mouth during the
747 simulation period.

748 **Figure 13.** Distribution of C_v at different times of the storm event: (a) clear water flow; (b)
749 initiation of debris flow; (c) channelized debris flow; (d) post hyperconcentrated/clear
750 water flow.

Table 1. Parameters used in the infiltration module verification.

Case	Vertical depth (cm)	α (cm ⁻¹)	θ_s	θ_r	k_s (cm/h)	q_a	q_b	γ (°)	Rainfall duration (h)
1	100	0.1	0.40	0.06	10	0.1	0.9	0	20
	100				1				
2	100	0.01	0.40	0.06	1	0.1	0.9	0	20
	100				10				
3	400	0.01	0.42	0.18	3.6	0	$0.4k_{st}$	40	20
	100		0.30	0.10	0.036				
4	400	0.01	0.42	0.18	3.6	0	k_{st}	40	20
	100		0.30	0.10	0.036				

Notes: α = constitutive parameter; θ_s = saturated water content; θ_r = residual water content; k_s = saturated permeability; q_a = antecedent rainfall intensity; q_b = rainfall intensity for time greater than zero; γ = slope angle. Parameters α , θ_s and θ_r are used in the constitutive relations between the hydraulic conductivity and moisture content and the pressure head (Srivastava and Yeh, 1991).

Table 2. Properties of four types of superficial materials.

Geological type	c' (kPa)	ϕ' (°)	γ_{sat} (kN/m ³)	K_s (m/s)	α (cm ⁻¹)	θ_s	θ_r
Vegetated land	10.5	37	21	1×10^{-6}	0.8	0.40	0.25
Bed rock	-	-	-	0	-	-	-
Loose soil deposit	4	37	21	1×10^{-5}	0.8	0.42	0.18
Riverbed	-	-	-	1×10^{-3}	-	-	-

Notes: c' = true cohesion of soil; ϕ' = friction angle of soil; γ_{sat} = unit weight of solid particles; K_s = saturated permeability of soil.

Table 3. Soil properties for debris flow simulation.

d_{50} (mm)	ρ_s (kg/m ³)	C_{v*}	s_b	τ_c (Pa)	K_e (m ³ /N-s)
35	2650	0.65	1	8.7	78.5×10^{-9}

Notes: d_{50} = mean grain size; ρ_s = density of solid particles; C_{v*} = volume fraction of solids in the erodible bed; s_b = degree of saturation of the erodible bed; τ_c = critical erosive shear stress; K_e = coefficient of erodibility.

Table 4. Constitutive (rheological) parameters for debris flow simulation.

α_1 (kPa)	β_1	α_2 (Pa·s)	β_2	K	δ_d	n
3.8	3.51	0.02	2.97	2500	0.02	0.16

Notes: α_1, β_1 = empirical coefficients for calculating τ_y ; α_2, β_2 = empirical coefficients for calculating μ ; K = laminar flow resistance coefficient; δ_d = deposition coefficient; n = Manning's coefficient.

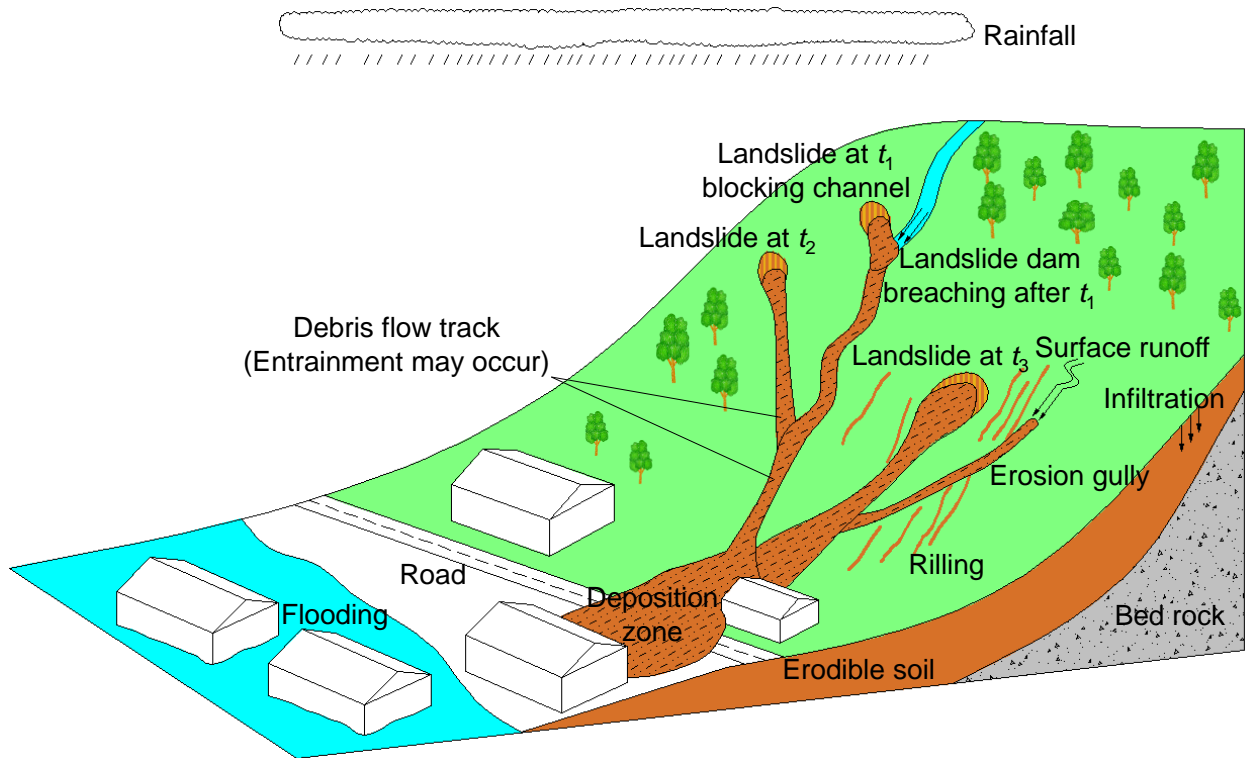


Figure 1. Conceptual model of a rain-induced debris flow and three typical initiation mechanisms of debris flows: bed erosion, transformation from landslide, and dam breach.

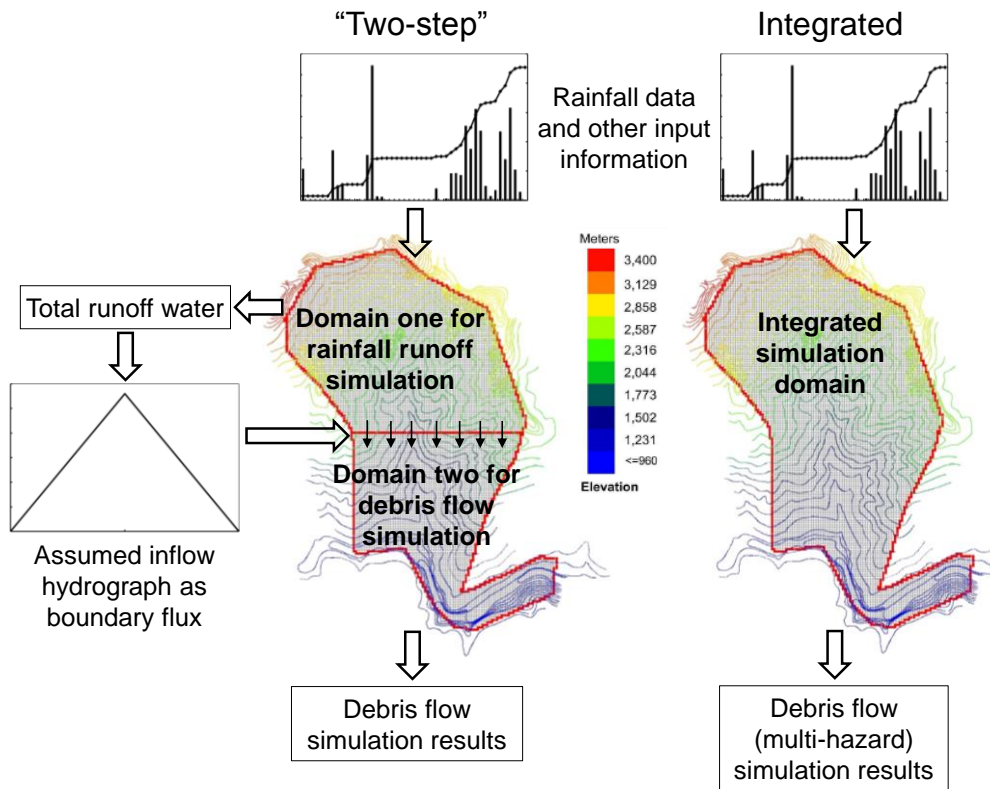


Figure 2. Comparison between “two-step” simulation and integrated simulation of rain-induced debris flows.

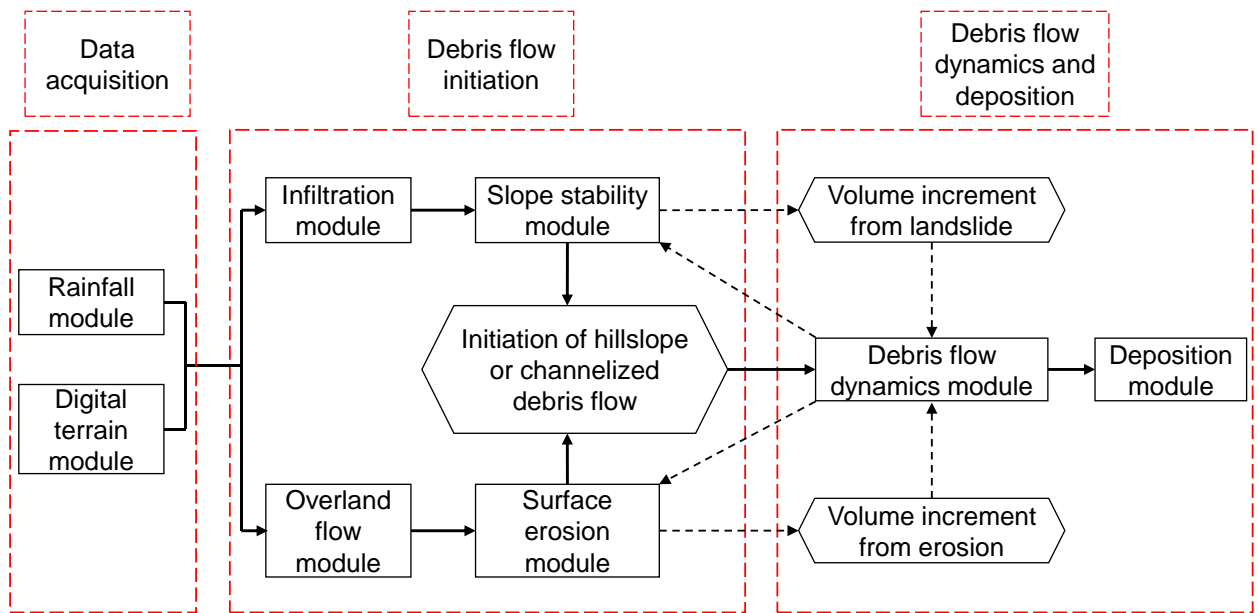


Figure 3. Framework of the integrated simulation of debris flows.

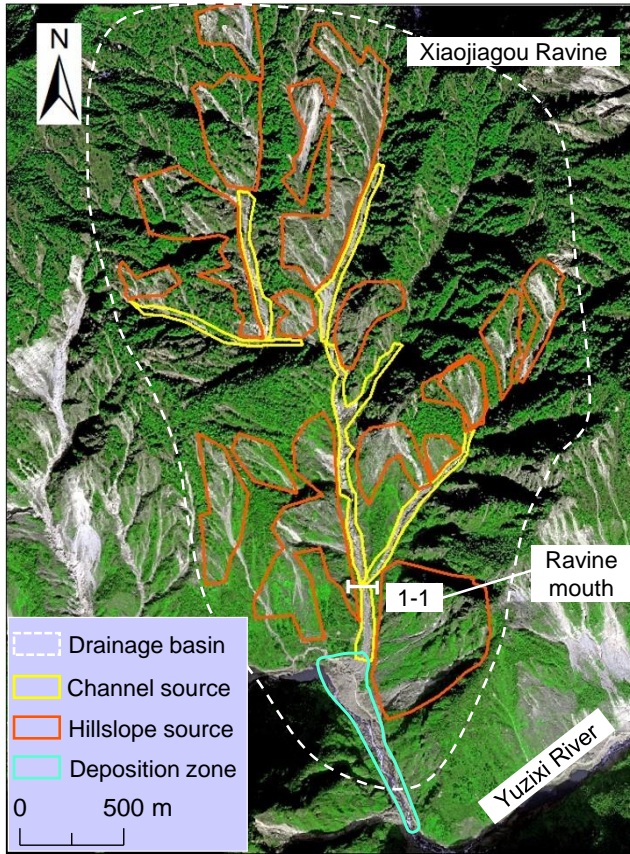


Figure 4. A satellite image of the study area taken shortly after the Xiaojiagou debris flow on 14 August 2010.

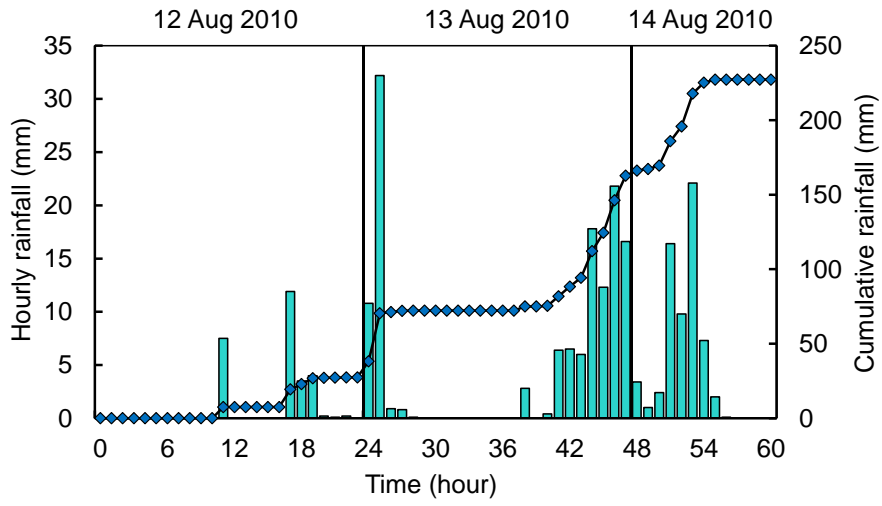


Figure 5. Rainfall process of the August 2010 rainstorm.

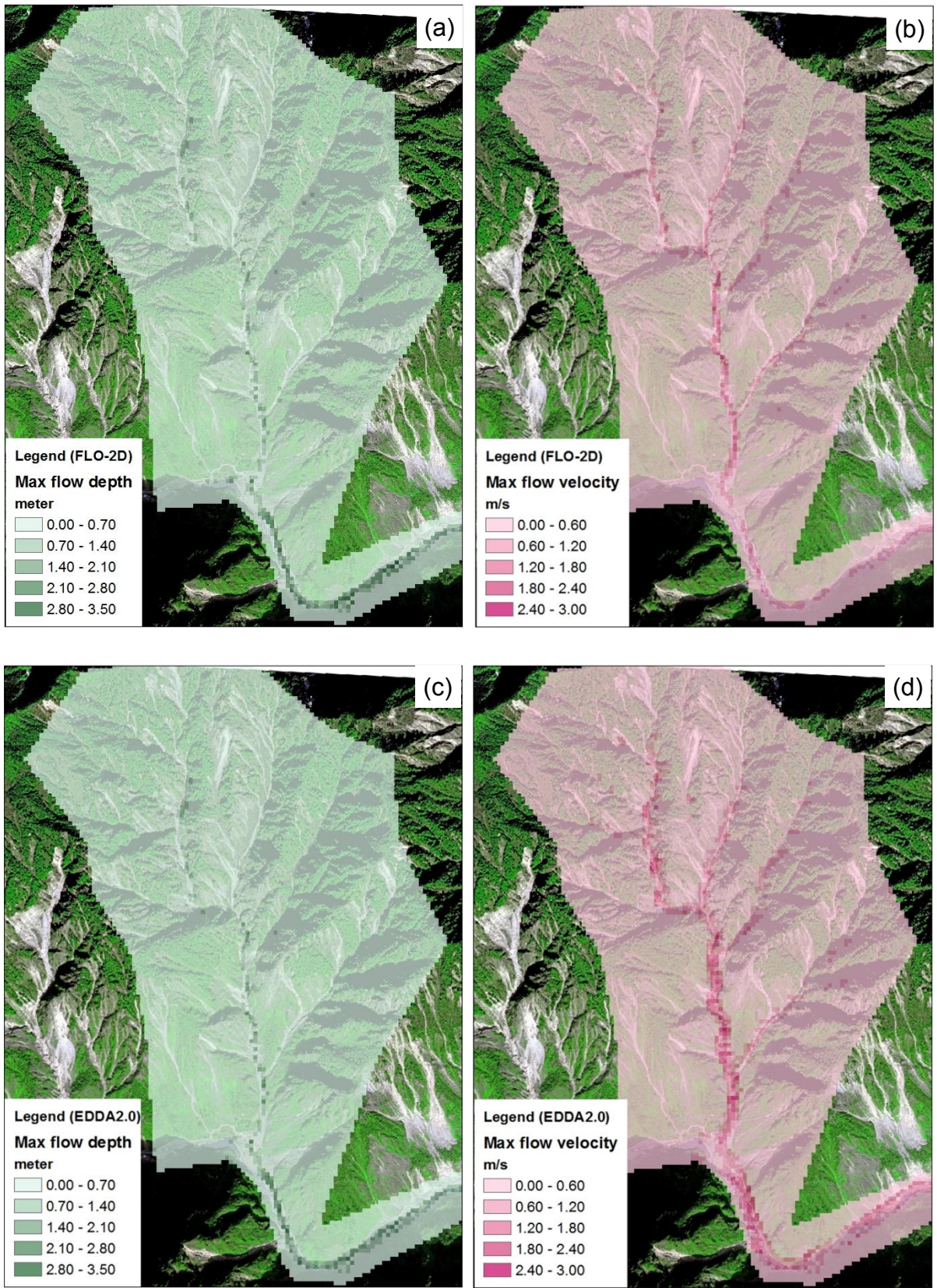


Figure 6. Comparison of the maximum surface runoff flow depths and flow velocities simulated using FLO-2D [(a) and (b)] and EDDA 2.0 [(c) and (d)].

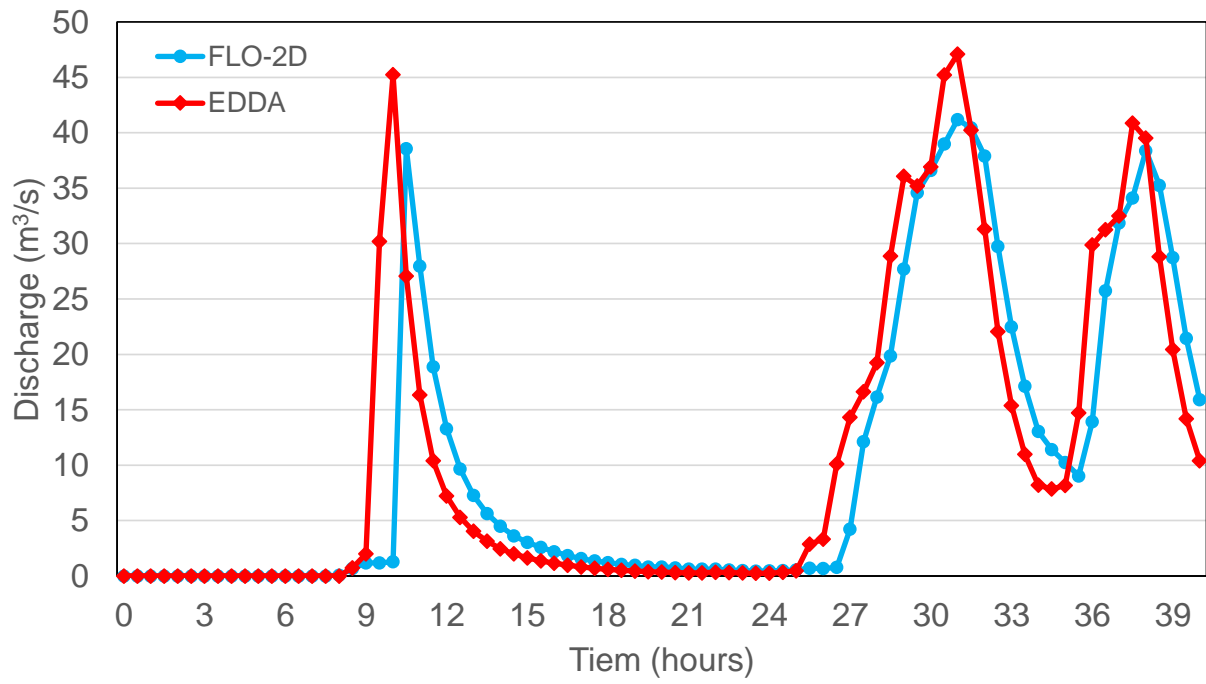


Figure 7. Comparison of the outflow hydrographs at the ravine mouth using FLO-2D and EDDA 2.0.

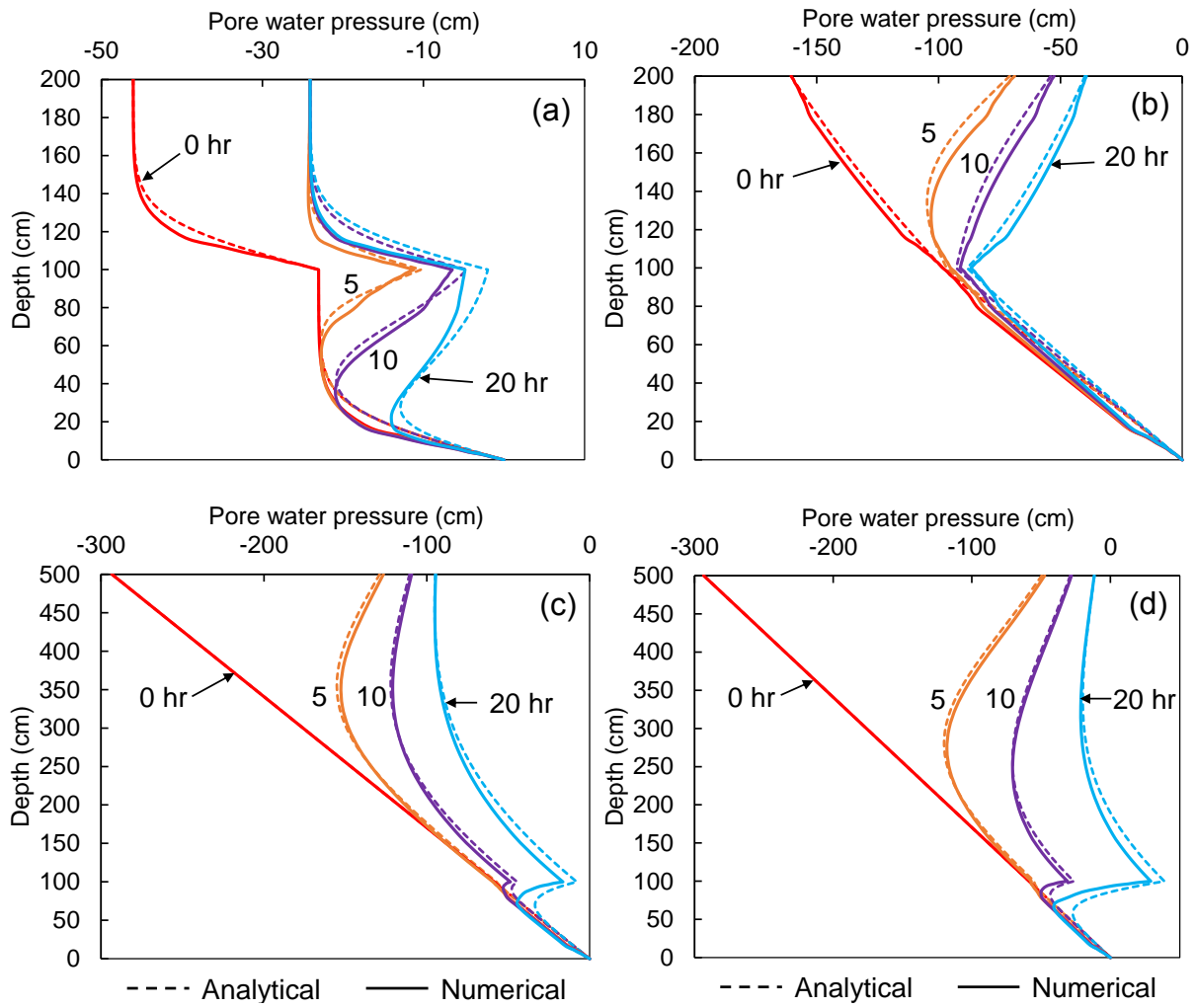


Figure 8. Pore water pressure profiles at various times: (a) Case 1; (b) Case 2; (c) Case 3; (d) Case 4.

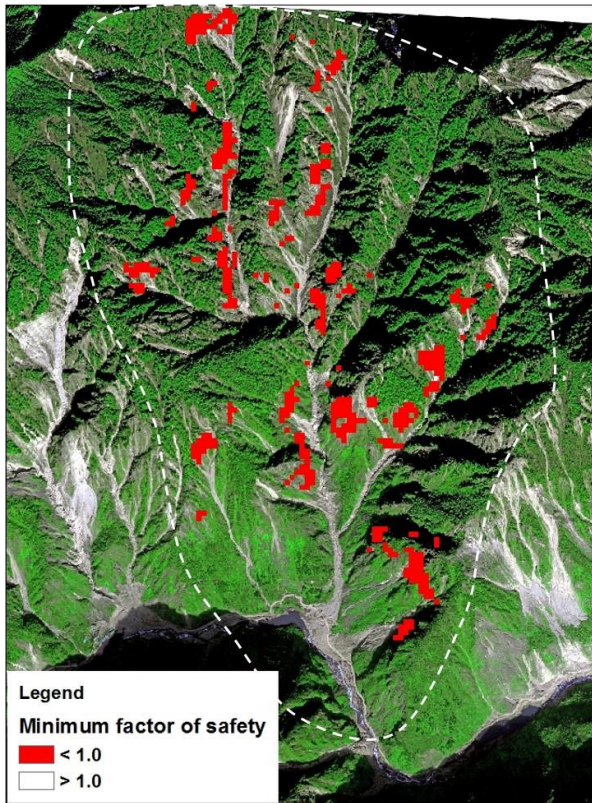


Figure 9. Computed unstable cells vs. landslide scars on the satellite image.

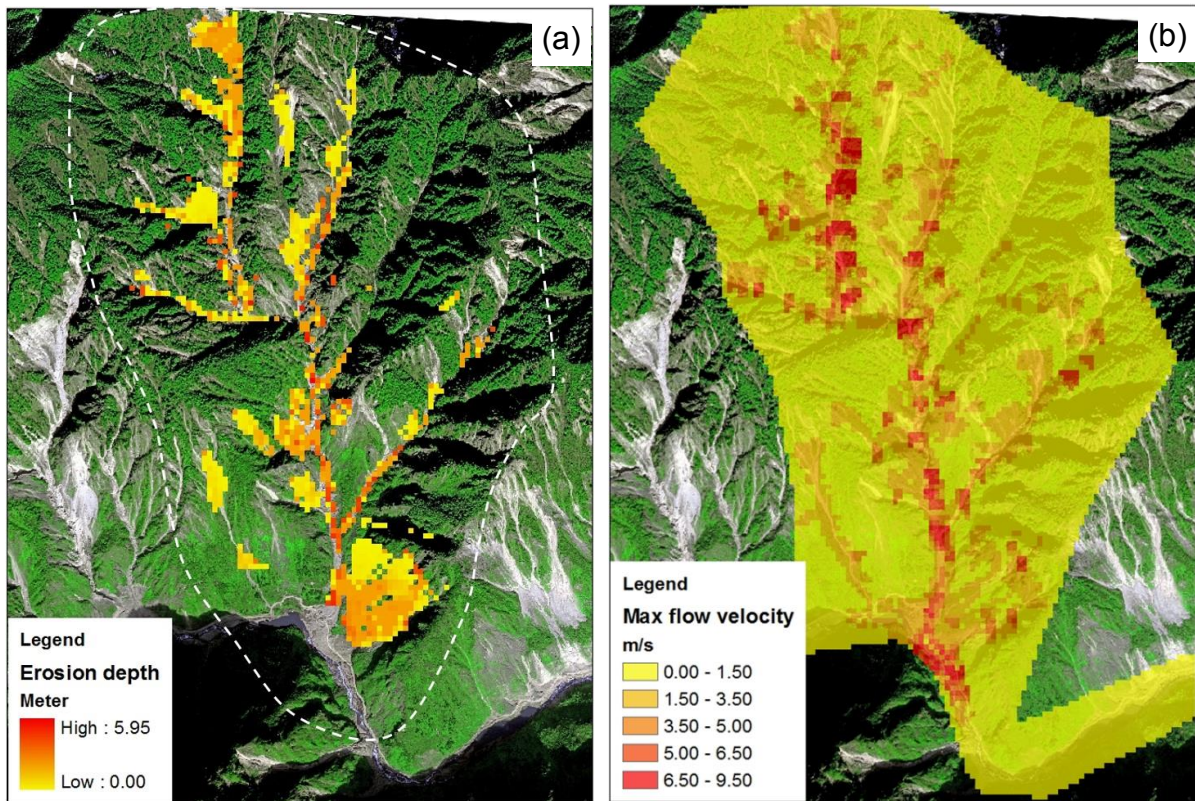


Figure 10. Simulation results of the Xiaojiagou debris flow: (a) final shape and depth of the erosion zone; (b) maximum flow velocity.

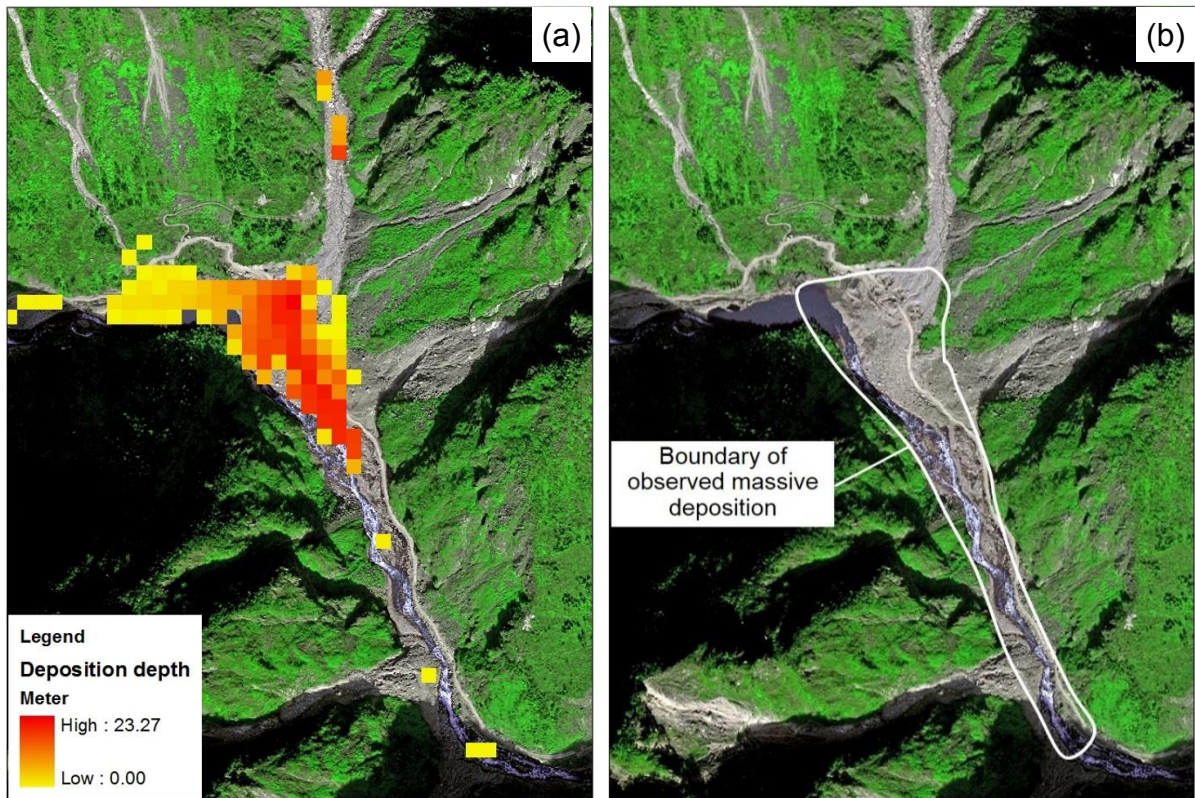


Figure 11. Comparison of the simulated and observed deposition zones: (a) simulation result; (b) enlarged view of the observed deposition area (Chen and Zhang, 2015).

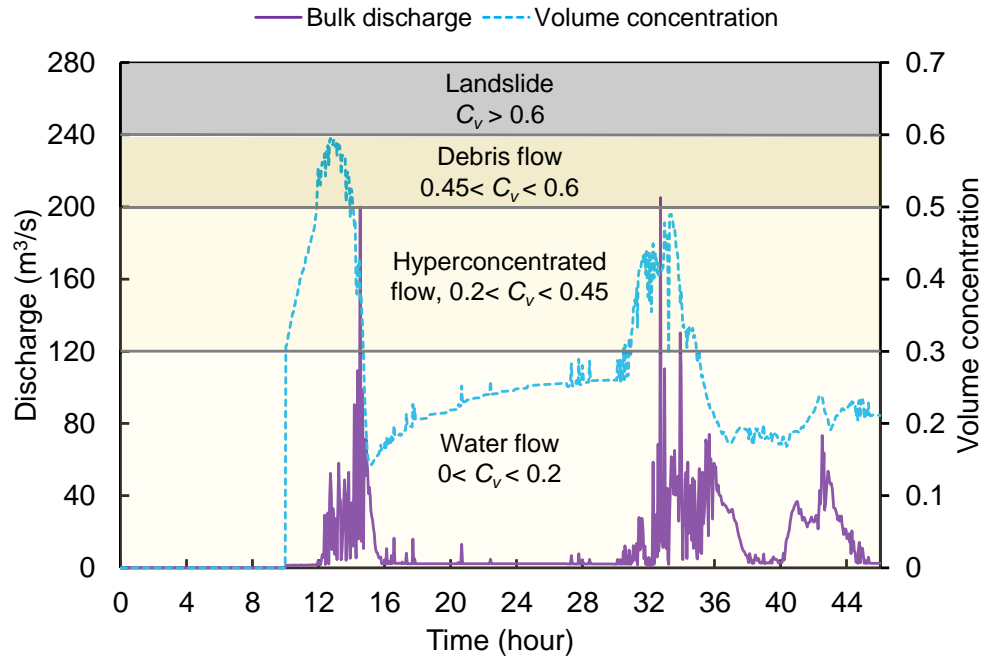


Figure 12. Outflow hydrograph and changes in C_v at the Xiaojiagou Ravine mouth during the simulation period.

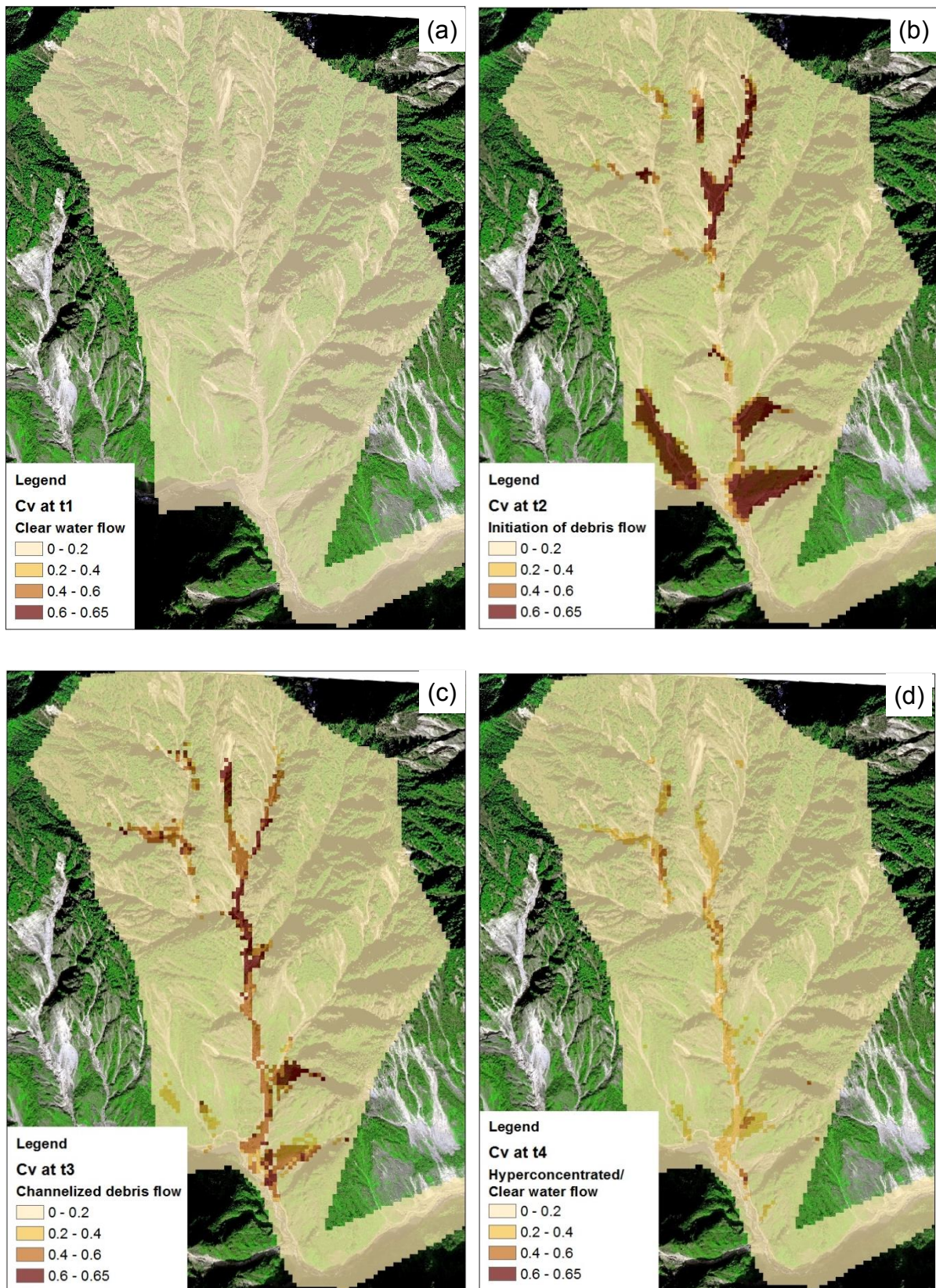


Figure 13. Distributions of C_v at different times of the storm event: (a) clear water flow; (b) initiation of debris flows; (c) channelized debris flows; (d) post hyperconcentrated/clear water flow.